RSC Advances

ROYAL SOCIETY OF CHEMISTRY

www.rsc.org/advances

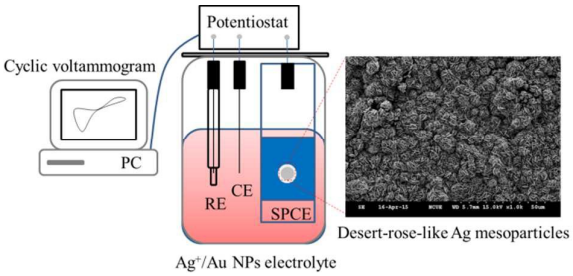

Desert-rose-like Ag mesoparticles prepared by cyclic voltammetric method possess excellence SERS-activity, reproducibility, thermal stability and aging behavior.

Journal Name

RSCPublishing

ARTICLE

Surface-Enhanced Raman Scattering-Active Desert-Rose-Like Ag Mesoparticles Prepared Using Cyclic Voltammetric Methods

You-Hong You, Yang-Wei Lin*, and Chung-Yu Chen

Cite this: DOI: 10.1039/xoxxoooooox

Received ooth January 2012,
Accepted ooth January 2012

DOI: 10.1039/xoxxoooooox

www.rsc.org/

Desert-rose-like Ag mesoparticles were deposited on a screen-printed carbon electrode substrate through a cyclic voltammetric process in aqueous $AgNO_3$ containing Au nanoparticles. The prepared mesoparticles were characterized using scanning electron microscopy, energy dispersive X-ray spectroscopy, surface-assisted laser desorption/ionization mass spectrometry, X-ray photoelectron spectroscopy, and high-resolution X-ray diffractometry. In addition, the potential for applying these mesoparticles in surface-enhanced Raman scattering (SERS) was investigated. The prepared mesoparticles exhibited a more intense SERS signal (34.3 times) than did irregularly shaped Ag particles because of their extremely intense local electromagnetic fields. The enhancement factor of 4-mercaptobenzoic acid molecules on these mesoparticles was approximately 10^5. Furthermore, SERS spectra of 4,4'-dimercapto-azobenzene, 5,5'-dithiobis-2-nitrobenzoic acid, and Cy3 dye modified DNA were obtained using these mesoparticles; moreover, hot spots for most of the enhanced SERS signals were easily obtained. The thermal stability and aging behaviour of the prepared Ag mesoparticles were higher than those of irregularly shaped Ag particles.

Introduction

Surface-enhanced Raman scattering (SERS) spectroscopy provides powerful and extremely sensitive analytical detection in biochemistry, chemical production, and environmental monitoring.[1-5] Because of the electromagnetic enhancement mechanism of metal nanoparticles (NPs), their surface morphologies remarkably affect SERS applications.[6, 7] Au or Ag particles of different shapes and sizes are currently widely investigated for developing a highly efficient SERS substrate. In particular, Au and Ag microstructures have been attracting increasing attention because their hierarchical characterization (surface roughness) is crucial in inducing a strong electromagnetic field enhancement for SERS.[8-12]

Hierarchical silver nanostructures can be obtained by template method. For example, Nakanishi and coworkers demonstrated that nanoflake Au surfaces can be fabricated by sputtering Au metal directly onto a thin film of self-assembled fullerene materials.[8] The enhancement factor (EF) of 4-aminothiolphenol (4-ATP) on Au nanoflakes was calculated to be 10^4. Choi and coworkers prepared a controllable flower-like Au nanostructure array through photolithography and electrodeposition.[9] The dependence of the SERS signal on the surface roughness of the flower-like Au nanostructure was demonstrated, and various molecules, including brilliant cresyl blue, benzenethiol, adenine, and DNA, were detected with high sensitivity. They successfully developed a well-ordered Au nanostructure on a large-scale SERS substrate. However, the expensive lithographic methodology appears to be necessary. Maboudian and coworkers presented an efficient, simple, and reproducible method for preparing a Ag nanodesert rose substrate based on the Ag galvanic displacement on Si.[10] Compared with evaporated flat Ag substrates, EFs of 1,2-bis(4-pyridyl)ethylene, 4-mercaptopyridine, and rhodamine 6G were 3×10^4, 2×10^5, and 2×10^{10}, respectively. A high concentration of F^- ions (0.6 M) was used during Ag galvanic displacement. To obtain perfect galvanic displacement results, Si chips were placed in a Ag plating solution for 24 h. Thus, this process is time intensive and unsuitable for developing environmentally benign green chemical processes.[13-15] Li and coworkers reported an Au nanoflake film replicated from a self-assembled dipeptide flower-like hierarchical architecture.[11] The EF of 4-mercaptobenzoic acid (4-MBA) molecules on the Au nanoflake surface was approximately 10^4. Although the flexibility and adaptability of this method are remarkable compared with those of conventional methods that use fixed templates, the size and shape of the dipeptide supramolecular structures must be controlled carefully to achieve high SERS sensitivity. In addition, a two-step method (preparing

dipeptide hierarchical assemblies and sputtering Au metal) for fabricating a SERS substrate is time intensive. In 2014, Xia and coworkers proposed a hierarchically flower-like Ag microstructure through the in situ reduction of Ag^+ ions by using a polyaniline component.[12] The rough surface of the Ag microstructure creates abundant interstitial sites, resulting in enhanced Raman signals (EF of 4-MBA molecules = 10^5). However, preparing a polyaniline/poly(vinyl alcohol) composite film requires at least 3 days. Furthermore, among the methods available for producing Ag flower-like structures, surfactants or templates may be required during the synthesis process.

One-step electrochemical synthesis and depostion is seen as a simple technique that provides versatility in tailoring the architecture of metals on the micro/nanoscale.[16-18] In this study, we demonstrate that desert-rose-like Ag mesoparticles can be deposited on screen-printed carbon electrode (SPCE) substrates through a cyclic voltammetric process involving aqueous $AgNO_3$ containing Au NPs. Because the rough surface and interlaced nanosheets of the desert-rose-like Ag mesoparticles create abundant interstitial sites, more hot spots for SERS with high sensitivity can be easily obtained. Therefore, these Ag mesoparticles provide a more intense SERS signal (34.3 times) than do irregularly shaped Ag particles. The EF of 4-MBA molecules on the desert-rose-like Ag mesoparticles was estimated to be 1.3×10^5. The growth mechanism, signal reproducibility, thermal stability, and aging behaviour of the prepared Ag structures were investigated. For demonstrating biomolecule sensing using the proposed Ag substrate, we detected single-stranded DNA through sequence-selective hybridization. To our knowledge, this is the first time that desert-rose-like Ag mesoparticles are synthesized and deposited simultaneously on a SPCE substrate through a cyclic voltammetric process, providing high SERS activity for biomolecule sensing. Furthermore, since SPCE is designated for mass production, the proposed fabrication procedure is able extend to disposable SERS-active substrates and hence the results open a useful methodology in the field of SERS-active substrates and electrochemical sensors.

Experimental sections

Chemicals

All chemicals, 4-MBA, 4-ATP, 5,5′-dithiobis-2-nitrobenzoic acid (DTNB), $AgNO_3$, $NaAuCl_4$, sodium citrate, sodium hydrogen phosphate, disodium hydrogen phosphate, and dimethyl sulfoxide, were of ACS grade and obtained from Sigma-Aldrich (Milwaukee, WI, USA). Sodium hydrogen phosphate (0.1 M) and disodium hydrogen phosphate (0.1 M) were prepared in phosphate buffer solution (PBS; 0.1 M; pH 7.4). DNA sequences were purchased from Genomic (New Taipei City, Taiwan). SPCEs were obtained from Zensor R&D (Taichung, Taiwan). Ultrapure water from a Milli-Q ultrapure system (Millipore, MA, USA) was used throughout the study.

Preparation of Au NPs

Different sizes of Au NP (diameter: 13, 32 and 56 nm) suspensions were prepared as described previously.[19, 20] In brief, a 50-mL aqueous solution of 4 mM sodium citrate was brought to a vigorous boil with stirring in a round-bottom flask fitted with a reflux condenser; 0.1 M $NaAuCl_4$ (0.5 mL) was then added rapidly to the solution. The solution was heated under reflux for another 8 min, during which time its color changed from pale yellow to deep red. The solution was cooled to room temperature while stirring continuously. The sizes of the Au NPs were verified through TEM analysis (H7100, Hitachi High-Technologies Corporation, Tokyo, Japan); the Au NPs appeared to be nearly monodisperse, with an average size of 13.2 ± 0.5 nm (100 counts). Sodium citrate (34 mM; 0.5 mL) was added rapidly to an aliquot of 0.25 mM $NaAuCl_4$ (50.0 mL) that was heated at 100 °C under reflux. Heating under reflux was continued for an additional 8 min, during which time the color changed to deep red. The solution was set aside to cool to room temperature. The as-prepared AuNP solution had a maximum absorbance at 528 nm (Evolution 200, Thermo Fisher, NY, USA), which is a characteristic surface plasmon resonance band for 32-nm Au NPs. The same process was applied for 56-nm Au NPs synthesis using a $NaAuCl_4$ (0.25 mM; 50.0 mL) and sodium citrate (34 mM; 0.3 mL).

Electrochemical synthesis of Ag structures

Cyclic voltammetry was conducted using a electrochemical workstation (CHI 600, CH Instruments, Austin, TX, USA). The three-electrode system consists of the SPCE as the working electrode (geometric area, 3.14×10^{-6} m^2), Ag/AgCl as the reference electrode, and platinum wire as the auxiliary electrode. Before initiating the electrochemical process, a bare SPCE was electrochemically cleaned by cycling the potential between −0.8 and 1.2 V vs. Ag/AgCl in PBS. Subsequently, the SPCE was preoxidized by applying a potential of 0.5 V for 600 s in PBS with stirring. The electrochemical synthesis of desert-rose-like Ag mesoparticles deposited on the SPCE was performed by cycling the potential from −0.3 to 0.3 V in aqueous $AgNO_3$ (10 mM) containing Au NPs (0.36 nM; diameter: 13 nm) at 2.5 mVs^{-1} for 15 scans. Under the same electrochemical conditions, irregularly shaped Ag particles deposited on the SPCE were fabricated without the addition of Au NPs in the electrolyte.

Characterization

The size and shape of the nanoparticles were characterized through scanning electron microscopy (SEM, JSM-6510, JEOL, Tokyo, Japan), and their compositions were determined through energy dispersive X-ray spectroscopy (EDS, Oxford Instruments, Oxfordshire, UK). High-resolution X-ray diffraction measurements were performed using a diffractometer (D8 SSS, Bruker, Bremen, Germany) with Cu

Kα radiation (λ = 0.15418 nm). Mass spectrometry was performed in the negative ion mode by using a Microflex matrix-assisted laser desorption/ionization time-of-flight mass spectrometer (Bruker Daltonics, Bremen, Germany). The SPCE substrate deposited Ag particles was directly plastered on a stainless steel and dried in air at room temperature for 1 h before recording the surface-assisted laser desorption/ionization mass spectra (SALDI-MS). X-ray photoelectron spectroscopy (XPS) was performed using a VG ESCA210 electron spectrometer (VG Scientific, West Sussex, UK).

General procedure for SERS analysis

For SERS measurements, Ag particles deposited on SPCE substrates were incubated in 4-MBA (1×10^5 M) for 30 min. The substrates were rinsed with ultrapure water and dried in vacuum in a dark atmosphere for 1 h at room temperature. Raman spectra were obtained using a confocal micro-Raman system (Thermo Scientific Inc, NY, USA). A 532-nm laser line with a laser power of 2 mW was used as the photoexcitation source and was operated for 10 s. Raman scattering signals were collected in backscattering geometry by using an objective lens with a magnitude of 10× and a numerical aperture of 0.25 and were detected using a spectrometer equipped with a thermoelectrically cooled charge-coupled-device detector.

Results and discussion

Characterization of the prepared Ag structures

Ag structures of various shapes were synthesized in the absence and presence of 13-nm Au NPs (0.36 nM) and with the following constant parameters: number of scans, 15; scan rate, 2.5 mV/s; scan potential range, −0.3 to 0.3 V versus Ag/AgCl; and $AgNO_3$ concentration, 10 mM. Figure 1a and b show the SEM image of Ag microstructures deposited on the SPCE surface in the absence of Au NPs. The surface of the deposited Ag structures was not well dispersed, and irregular islands with a low Raman activity were observed (discussed later). The EDS spectrum of the irregularly shaped Ag structures confirmed the existence of only Ag atoms (Figure S1a). Au NPs (300 μL, 15 nM, diameter 13 nm) were added to $AgNO_3$ (12 mL, 10 mM) under the same cyclic voltammetry conditions; the resulting surface morphology of the deposited Ag structures changed markedly (Figure 1c). The surface morphology of the Ag structures exhibited well-dispersed, and desert-rose-like mesoparticles with a high Raman activity, resulting from the abundant interstitial sites with a size less than 100 nm (Figure 1d). These like Ag mesoparticles, composed of intertwined plates, exhibited spiky and sharp features and are thus composed of areas characterized by a strong electromagnetic field enhancement because of the interaction of light with the plasmonically active structures. Consequently, the corresponding SERS performance increases. In addition, the EDS spectrum of the desert-rose-like Ag mesoparticles confirmed the existence of Ag atoms (Figure S1b). The crystal structure and phase composition of both Ag structures were further characterized through XRD (Figure S2). Peaks at 2θ = 38.1°, 41.2°, and 64.5° corresponded to diffractions from the (111), (200), and (220) lattice planes, respectively, of face-centered-cubic Ag, affirming the existence of pure crystalline Ag structures.

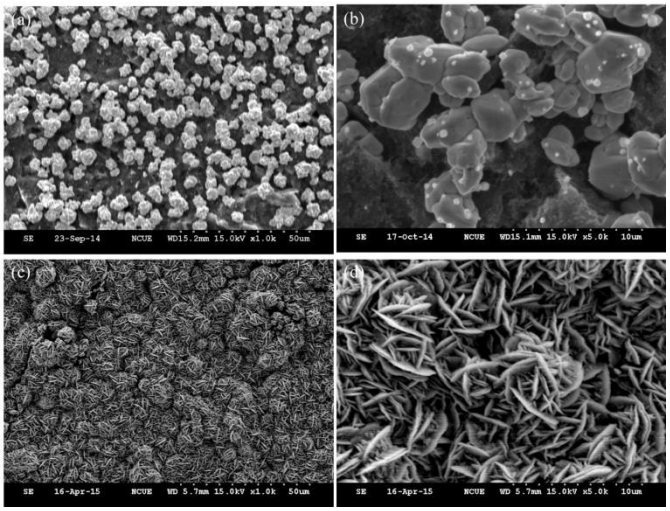

Figure 1. Scanning electron microscopy (SEM) images of the (a, b) irregularly shaped Ag particles and (c, d) desert-rose-like Ag mesoparticles on the SPCE surface.

To further confirm the existence of only Ag atoms on both Ag structures, the surface components and oxidation states of both Ag structures formed on the SPCE substrate were examined through SALDI-MS and XPS. Figure S3 presents the SALDI-MS spectra of the irregularly shaped Ag particles and desert-rose-like Ag mesoparticles. The signals at m/z 106.904 and 108.949 were assigned to $[Ag_1]^+$ (Figure S3a). The difference in the m/z ratio between the other signals was approximately 12 because of the presence of the SPCE substrate, indicating that Ag particles were deposited onto the SPCE substrate. Figure S3b shows that $[Ag_1]^+$ signals were obtained at m/z 106.431 and 108.462, indicating the absence of Ag/Au structures on the SPCE substrate. Figures S4a and b show the XPS spectra of irregularly shaped Ag particles and desert-rose-like Ag mesoparticles, respectively. The Ag signal is clearly seen in the spectra; the doublet peaks at 367.7 and 374.1 eV can be assigned to Ag(0). These results further confirmed the existence of only Ag atoms on both structures.

SERS performances of the prepared Ag structures

SERS is a powerful analytical tool for the quantitative analysis of target analytes in life sciences, environmental sciences, and medicine.[1-5] The surface morphology and nanostructure of the substrate crucially influence this technique. As mentioned previously, desert-rose-like Ag mesoparticles have a unique morphology and rough surface, rendering them suitable active substrates for SERS. To evaluate SERS performance, 4-MBA was used as a model

molecule because it forms a self-assembled monolayer on the Ag surface and has been thoroughly studied using SERS.[21] Figure 2 shows the SERS spectra of 4-MBA on irregularly shaped Ag particles and desert-rose-like Ag mesoparticles. The irregularly shaped Ag particles exhibited a low-intensity SERS signal. The peak intensities of the desert-rose-like Ag mesoparticles were considerably higher than those of the irregularly shaped particles. The two strong bands at 1582 and 1075 cm^{-1} dominated the SERS spectrum; these were assigned to ν8a aromatic ring vibrations and ν12 aromatic ring vibrations with C–S stretching characteristics, respectively.

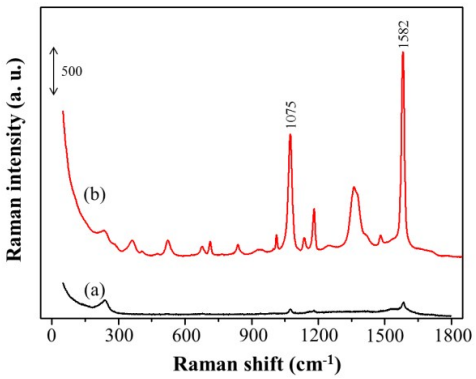

Figure 2. SERS spectra of 10^{-5} M 4-MBA of the (a) irregularly shaped Ag particles and (b) desert-rose-like Ag mesoparticles.

The surface roughness and surface area of the Ag structures increasing the electromagnetic field enhancement and a high number of adsorption sites, respectively, lead to an increase in the SERS intensity. To examine the effect of electromagnetic field enhancement on surface roughness, the surface areas of the irregularly shaped Ag particles and desert-rose-liked Ag mesoparticles on the SPCE substrate were measured through cyclic voltammetry in $Pb(NO_3)_2$ (5 mM), $HClO_4$ (1 mM), and $NaClO_4$ (0.1 M) at a scan rate of 10 mV/s and by assuming that a charge of 136 μCcm^{-2} was passed for stripping the Pb monolayer.[22] Consequently, the surface area of the desert-rose-like Ag mesoparticles deposited on the SPCE substrate was 10 times higher than that of the irregularly shaped Ag particles. However, Raman intensity at 1582 cm^{-1} of the desert-rose-like Ag mesoparticles showed a 34-fold increase compared with that of the irregularly shaped Ag particles (Table S1), meaning that the increment in the surface area does not correspond to the increase in the SERS intensity, and that a high SERS enhancement effect is attributable to the electromagnetic field enhancement effect of the geometrical characteristics of the desert-rose-like Ag mesoparticles. The surface morphology image in Figure 1 supports our hypothesis. Roughness factor (R_f) is defined as the ratio of the true surface area, obtained through electrochemical methods, to the geometric area.[22] The R_f of the irregularly shaped Ag particles and desert-rose-like Ag mesoparticles were 0.64 and 6.69, respectively, suggesting that cyclic voltammetry in the presence of Au NPs and Ag^+ ions roughened the surface of the Ag structures, thereby improving the SERS enhancement because of the electromagnetic field enhancement effect.

Recent studies revealed that the SERS enhancement effects of metal NPs with random roughness can be greatly improved due to electromagnetic enhanced of the optical field at rough metallic surface.[23-25] For example, ultrasensitive SERS using star-shaped Au NPs was demonstrated by Alvarez-Puebla and coworkers.[24] By sandwiching the 15NAT molecules between the tips of star-shaped Au NPs and a planar Au surface, a zeptomol detection limit for 15NAT was found in their study. Wang and coworkers reported the Ag nanospheres with sharp tips on their surface exhibit much better Raman scattering enhancement than non-agglomerated spherical Ag NPs.[25] All of these studies indicated that the SERS enhancement effect was markedly improved *via* enhanced electromagnetic fields between the gaps of the two NPs or the NPs with roughness surface. Therefore, a higher SERS signal intensity of 4-MBA adsorbed on the desert-rose-like Ag mesoparticles with random roughness can be observed.

The growth mechanism of desert-rose-like Ag mesoparticles

Following cyclic voltammetry in the presence of Au NPs and Ag^+ ions over various times by SEM, the increase in the coverage of the substrate and the growth of the particles were clear (Figure S5a–f). The desert-rose-like structures appeared after 1 min. However, they were not easily visible because of the low surface coverage. After electrodeposition for 15 min (Figure S5d), a small plate-shaped structure parallel to the substrate plane is formed. This structure is connected to other interpenetrating structures (parallel and perpendicular to the substrate plane), which ultimately form the desert-rose-like structures. The ongoing growth of the individual structures and the resulting increase in the coverage of the substrate were more clearly visible after 30 min than after 15 min. As mentioned previously, the effect of electromagnetic field enhancement on surface roughness, which produces the desert-rose-like Ag mesoparticles, is also a factor that increases SERS intensity. As shown in Figure S6, both the R_f and SERS intensities of the desert-rose-like Ag substrates increased with increasing electrodeposition duration.

We know that sodium citrate acted as the reducing and capping agent for reducing Au^{3+} ions and then stabilizing the as-prepared spherical Au NPs. Excess sodium citrate may be helpful for fabricating desert-rose-like Ag mesoparticles during an electrochemical process. For proving our assumptions, Au NP suspensions were centrifuged for obtaining supernatants and precipitates. Figure S7 shows that meatball-like Ag particles and desert-rose-like Ag mesoparticles were obtained when the precipitates and supernatants of Au NPs were used for fabricating Ag mesoparticles, respectively. It indicates that sodium citrate determines on the morphology of the Ag structures. Figure S8 shows different surface morphologies and SERS spectra of 4-MBA adsorbed onto Ag substrates fabricated by 10 mM Ag^+

depsotion solutions contianing various concentrations of sodium citrate. Furthermore, the surface density of desert-rose-like Ag mesoparticles using sodium citrtate is lower than that using Au NP suspensions (Figure S8c vs. Figure 1c). In addition, the Ag/Au nanocomposites can be found in the Ag^+ depsotion solutions containg Au NP suspensions (Figure S9). In summary, Au NP can regulate the transfer of the electrons through formation of Au/Ag nanocomposites and decrease the growth rate of Ag mesoparticles. This affects both the size and amount of Ag mesoparticles on SPCE substrates. However, in the absence of Au NPs, too big Ag mesoparticles would accumulate on the surface of SPCE, which adversely affects the light absorption, resulting in a decrease in the SERS efficiency. Therefore, the different SERS signals were caused by the different morphology and surface density of Ag microstructures on SPCE.

Based on our aforementioned results, we propose a possible growth mechanism for the desert-rose-like Ag mesoparticles through particle-mediated growth.[26-28] In the particle-mediated growth process, the particles do not simply aggregate with each other. In the first stage, Ag^+ ions are electroreduced to Ag atoms through a cyclic voltammetric process (i.e., scanning from +0.3 to −0.3 V vs. Ag/AgCl) and by using sodium citrate (Au NP suspension). The concentration of Ag atoms on the SPCE surface gradually increases as the reaction proceeds. In the second stage, as the concentration of the Ag atoms increases, the supersaturation point of nucleation is reached, and the atoms aggregate to form a nucleus, thus producing Ag NPs on the SPCE surface. Simultaneously, the concentration of Ag atoms decreases with increase in the Ag NP concentration. Consequently, the Ag NP formation stops when the concentration of Ag atoms decreases to a level lower than the supersaturation point of nucleation. Sodium citrate prevents Ag NP oxidation during cyclic voltammetry scanning to the positive side. At the same stage, Ag NP imvolves an action, oriented attachment, in which the Ag NP align along a common crystallographic direction in order to minimize the intrface energy.[27] In the third stage, the remaining Ag^+ ions are electroreduced and electrodeposited on the oriented attachment Ag NPs to form spherical mesoparticles when the cyclic voltammetry process is scanned again to the negative side. In this system, Au NP acts as a role for the electroredured modifier for decreasing the growth rate of the desert-rose-like Ag mesoparticles.

Optimization of SERS performance

Additional assay parameters were evaluated to further optimize the experimental protocol. The effect of Au NP size was investigated by using 32 and 56 nm Au NPs (Figure S10). The SERS intensity of the 4-MBA molecules decreased with increasing Au NP size, possibly because of the different surface morphologies of the Ag structures, which reduces the SERS intensity. To confirm this hypothesis, the surface morphologies of different Ag structures were obtained through SEM. The desert-rose-like Ag structures were not obtained for the 32-nm and 56-nm Au NPs. Therefore, Au NPs of diameter 13 nm was determined as the optimal candidate for additional investigations.

To measure the relative intensity, we used the normalized Raman intensity, which is calculated as the ratio of the strongest intensity of 4-MBA adsorbed on the desert-rose-like Ag mesoparticles to that of 4-MBA adsorbed on the irregularly shaped Ag particles. Thus, the normal Raman scattering intensities need not be corrected to account for differences in the sampling geometry and scattering phenomenon.[29] Concentrations of Au NPs ranging from 0.18 to 1.8 nM (Figure S11a) were tested, and the normalized Raman intensity of 4-MBA molecules increased with increasing Au NP concentration up to 0.36 nM and reduced with further increase in the concentration. This is probably because of the instability of the Au NPs at high concentrations during the electrochemical process, which hinders the formation of the desert-rose-like Ag structure. Thus, the optimal Au NP concentration was determined to be 0.36 nM.

To examine the effect of the preoxidation potential, potentials ranging from 0.25 to 10 V were considered. As shown in Figure S11b, the maximum normalized Raman intensity of 4-MBA molecules was obtained when the oxidation potential was 0.5 V. At a high preoxidation potential, more hydroxyl groups are produced on the SPCE surface, favoring the adsorption of Ag^+ ions. In addition, the hydroxyl groups act as electron donors, leading to easy formation of large Ag mesoparticles. However, the adsorption of large structures on the SPCE surface is difficult because of the reducing normalized Raman intensity. Therefore, a preoxidation potential of 0.5 V was applied for additional experiments. The influence of the number of deposition scans and deposition scan rates were studied (Figure S11c and d). A high number of scans and high scan rate for cyclic voltammetry caused the excessive growth of Ag mesoparticles, making adsorption onto the SPCE surface difficult and leading to a reduction in the Raman intensity of 4-MBA molecules. Therefore, the optimal number of scans and the optimal scan rate were 15 and 2.5 mV/s, respectively.

Figure 3a shows the Raman spectra when a series of 4-MBA solutions of different concentrations were tested at the optimal conditions. The ν_{12} aromatic ring vibrations corresponding to the C–S stretching of the 4-MBA molecules were obtained at a concentration of 5×10^{-8} M. At this concentration, 4-MBA did not show any characteristic peaks; thus 10^{-9} M was considered the limit of quantify (LOQ) for 4-MBA molecules (ν_{8a} aromatic ring vibrations at 1582 cm^{-1} were obtained). A linear relationship was obtained from the plot of the Raman intensity at 1582 cm^{-1} versus the 4-MBA molecule concentration in a range 1.0 nM–0.1 μM (R^2 = 0.9956; Figure 3b).

EFs for the irregularly shaped Ag particles and desert-rose-like Ag mesoparticles were calculated using a detectable signal (Table S1) by using eq. (1):

$$\mathrm{EF} = \frac{I_{SERS}/N_{surf}}{I_{bulk}/N_{bulk}} \quad (1)$$

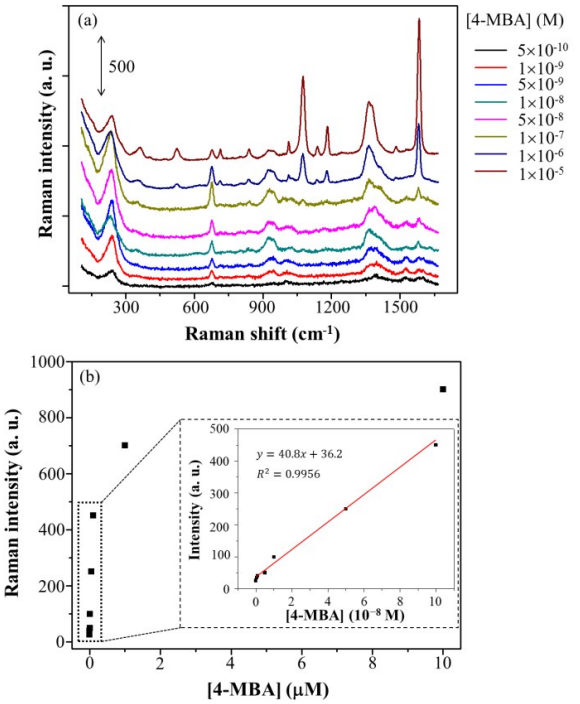

Figure 3. (a) SERS spectra of different concentrations of 4-MBA adsorbed on the desert-rose-like Ag mesoparticles. (b) Plots of the Raman intensity of 4-MBA on desert-rose-like Ag mesoparticles as a function of 4-MBA concentration.

where I_{SERS} and I_{bulk} are Raman intensities at 1582 cm^{-1} of the Ag structures and bulk, respectively. N_{surf} was numbers of 4-MBA molecules adsorbed on SPCE substrate, which is obtained under the assumption that the bonding density of 4-MBA molecules at the self-assembled monolayer is 0.5 $nmolcm^{-2}$.[7] As stated previously, the SERS active Ag structure surface area was measured using cyclic voltammetry. N_{bulk} defined as the numbers of 4-MBA molecules for the 4-MBA powder is 2.0×10^{12}, which is approximated using the molecular density of 4-MBA (1.346 gcm^{-3}) and laser spot size (approximately 10 μm in diameter and approximately 10 μm in depth). EFs were calculated using the intensities of peaks at 1582 cm^{-1}. Accordingly, EFs of the irregularly shaped Ag particles and desert-rose-like Ag mesoparticles were 2.0×10^4 and 6.5×10^4, respectively. These values are based on the assumption that the Ag surface is completely covered by 4-MBA molecules. In fact, whether a surface is completely covered by 4-MBA molecules can be determined through an electrochemical experiment by using $K_3Fe(CN)_6$ as the active probe.[30-32] The cover degree is described by hindrance (B), which is calculated using eq. (2):

$$B = 1 - \left[i_p^{ox}(4MBA) \Big/ i_p^{ox}(Ag) \right] \quad (2)$$

The B values for the irregularly shaped Ag particles and desert-rose-like Ag mesoparticles were calculated as 0.8 and 0.5, respectively, meaning that 80% of the irregularly shaped Ag surface and 50% of the desert-rose-like Ag surface were covered by 4-MBA molecules. Thus, EFs of the irregularly shaped Ag particles and desert-rose-like Ag mesoparticles were 2.5×10^4 and 1.3×10^5, respectively. These results are comparable to those of the previously reported metal SERS substrates.[11, 12]

Precision, thermal stability, and aging behavior

To test the reliability of the desert-rose-like Ag mesoparticles as a potential SERS substrate, the intra- and interday reproducibility of the Raman intensities at 1075 and 1582 cm^{-1} were measured. Figure S12 shows the results of Raman mapping of 4-MBA on three batches of desert-rose-like Ag substrates, demonstrating its high reproducibility. Table S2 also presents the results of intra- and inter-day precision. Small intensity fluctuations are attributable to the variations during the adsorption of 4-MBA molecules (relative standard deviation (RSD%): Intra-day, <4.1%, Inter-day, <6.7%). Nevertheless, the SERS intensities were relatively stable, indicating that the formed SERS substrate is ideal because of the controllability of the proposed electrochemical process.

Because a longer acquisition time (>2 h) was used for obtaining a satisfactory spectra, the destructive thermal effect of the proposed substrates on the SERS capability were evaluated under long-term laser irradiation. Thermogravimetric analysis of the 10% weight loss of 4-MBA molecules was conducted at 200 °C. At 150 °C, the weight loss was only 5%, indicating that 4-MBA slightly decomposed at high temperatures. Figure S13 shows the Raman spectra of 4-MBA adsorbed on the irregularly shaped Ag particles at 80 °C. The characteristic peak of 4-MBA was not observed clearly at temperatures higher than 80 °C. This reduction in the SERS capability was improved in the desert-rose-like Ag mesoparticles. Figure S14 presents the Raman spectra of 4-MBA adsorbed on the desert-rose-like Ag mesoparticles at 25 °C, 80 °C, 100 °C, 150 °C, and 200 °C. When the temperature was increased from 25 °C to 80 °C, the intensities of the characteristic Raman peaks of 4-MBA were increased (green curve in Figure S14). As shown in the literature, substrate-temperature dependences of SERS below and above room temperature were widely investigated through theoretical and experimental studies.[33-35] We propose a possible mechanism in which high temperature induced a small but significant particle diffusion in closely spaced Ag mesoparticles. The result of the shifting changed the average interparticle distance, which subsequently increases the electromagnetic coupling between the Ag mesoparticles, and in turn causes an increase in the SERS intensity. When the temperature was increased to 200 °C, the characteristic Raman bands of 4-MBA could not be defined (black curve in Figure S14). The SERS capability of the desert-rose-like Ag mesoparticles increased at high temperatures, and the operating temperature can be as high as 150 °C. The SEM images in Figure S14 indicate that the reduction in the SERS capability at 200 °C is ascribable to the

destruction of the Ag mesoparticles. The originally desert-rose-like Ag mesoparticles become smoother, and some thin films were observed due to annealing effects. These results indicate that the loss in SERS effects for the desert-rose-like Ag microstructures can be attributed to the decrease of the electromagnetic field enhancement effect, as revealed from the SEM images.

To investigate the influence of the irregularly shaped Ag particles and desert-rose-like Ag mesoparticles on the aging behaviors of the SERS active substrate, both Ag structures were placed in an atmosphere of 50% RH and 20% O_2 at 25 °C for 30 days. Figure S15 demonstrates the reduction in the Raman intensity as a function of aging time. In addition, we used the normalized Raman intensity, calculated as the ratio of the peak intensity of 4-MBA at 1582 cm^{-1} on the first day to that at any other time. Therefore, account for differences in the sampling geometry and scattering phenomenon is unnecessary. The aging test indicated that the SERS capability of the irregularly shaped Ag particles reduced after 1 day. After 30 days, the normalized intensity of the irregularly shaped Ag particles reduced to only 5%. However, the normalized intensities of 4-MBA adsorbed on the desert-rose-like Ag mesoparticles were maintained at 65%. This revealed that the desert-rose-like Ag mesoparticles can provide a superior SERS performance with respect to stability and durability.

Applications of desert-rose-like Ag structures

Figure S16 shows the SERS spectrum of 4,4′-dimercapto-azobenzene (DMAB) and DTNB on the desert-rose-like Ag mesoparticles deposited on the SPCE substrate. The samples were incubated in ethanolic (10^{-5} M) 4-ATP and DTNB for 1 h and rinsed to remove excess solvent. On the surface of the desert-rose-like Ag mesoparticles, 4-ATP was photochemically converted to DMAB.[36] The Raman peaks of DMAB at 1072 and 1576 cm^{-1} were assigned to ring breathing coupled with C–S and C–C stretching vibrations, respectively. The Raman peaks at 1142 and 1188 cm^{-1} were assigned to C–N stretching and C–H bending vibrations, respectively. The Raman peaks at 1391, 1437, and 1472 cm^{-1} were assigned to N–N stretching, C–C stretching and C–H bending vibrations, respectively. The Raman spectrum of DTNB was dominated by the strong peak at 1332 cm^{-1}, which was assigned to the symmetric stretching of the nitro group. The Raman peak at 1558 cm^{-1} was assigned to an aromatic ring mode. The SERS intensities can be explained in terms of geometry. A linear relationship was obtained from the plot of Raman intensity as a function of the concentration of DMAB and DTNB in a range 10 nM–1 μM (R^2 = 0.9106) and 50 nM–1 μM (R^2 = 0.9675), respectively.

For additional applications of the desert-rose-like Ag mesoparticles in biomolecule detection, the capability of the desert-rose-like Ag mesoparticles to detect single-stranded DNA was evaluated. Figure 4a demonstrates the schematic of DNA immobilization and hybridization on the desert-rose-like Ag mesoparticles. A thiol-terminated DNA strand (5′-CCAGATACTCACCGG-SH-3′), which can recognize the fumarylacetoacetate hydrolase (FAH) gene, was used as the probe.[37] Mutation of this gene is accomplished with a human genetic disease, hereditary tyrosinemia type 1. Through strong Ag–S covalent bonding, the probe was immobilized on the surface of the desert-rose-like Ag mesoparticles at room temperature for 12 h. A 15-mer oligonucleotide was used as the target strand, and Cy3 was modified at the end of the target for the Raman signal (5′-Cy3-CCGGTGA*G*TATCTGG-3′). Figure 4b reveals that our probe was sensitive to this target gene, with an LOD of 2.6 nM (S/N = 3). A linear relationship was also obtained from the plot of Raman intensity (1465 cm^{-1}) as a function of the concentration of target DNA strand over the range of 10 nM–10 μM (R^2 = 0.97). A featureless spectrum was obtained when a noncomplementary target DNA strand was used. Thus, desert-rose-like Ag mesoparticles have great potential for detecting single-stranded DNA.

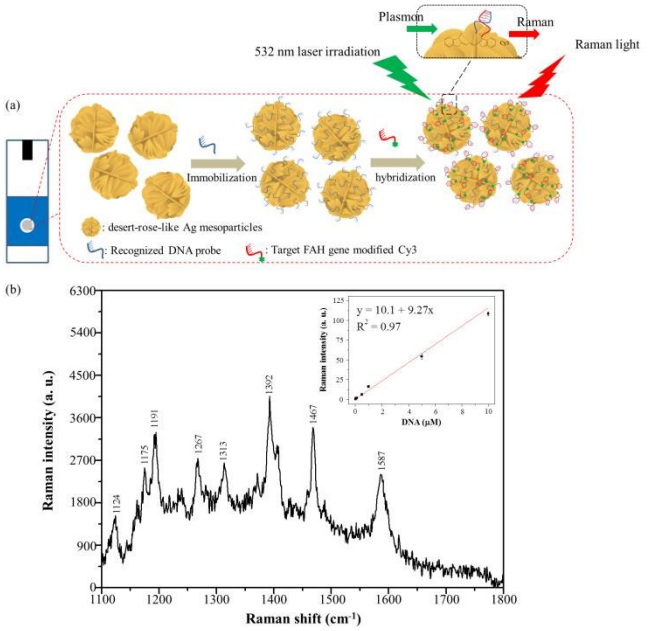

Figure 4. Demonstration of DNA sensing. (a) Schematic of DNA immobilization and hybridization on the desert-rose-like Ag mesoparticles. (b) Raman spectra of Cy3 obtained using a target single-stranded DNA (FAH gene) attached to the desert-rose-like Ag mesoparticles. Inset: Plots of Raman signal intensity versus DNA concentration.

Conclusions

We demonstrated a cyclic voltammetric method for synthesizing desert-rose-like Ag mesoparticles deposited on the SPCE substrate and their applications in SERS. The formation of abundant interstitial sites resulted in a rough surface, and the interlaced nanosheets of the desert-rose-like Ag mesoparticles exhibited a high sensitivity for SERS measurements. This preparation protocol possessed several attractive features compared with previously reported approaches (Table S3); their advantages are as follows: (1) low cost and simple: expensive enzymes, organic solvents, complicated preparation of templates, and sophisticated

photolithographic techniques are not required; (2) quick and inexpensive: cyclic voltammetric process only required 60 min; (3) reliability and reproducibility: intraday and interday RSD% are less than 4.1% and 6.7%, respectively; (4) robust and durable: the desert-rose-like Ag mesoparticles reduce the loss of the SERS signals at 150 °C and can withstand aging for 30 days; and (5) practicality: high-quality SERS spectra were obtained for various molecules (4-MBA, DMAB, DTNB, and Cy3-DNA). Because discovering highly SERS-active substrates continues to be a frontier, the facile method proposed in this study can lead to a new model in designing SERS active substrates. In addition, the Ag mesoparticles deposited on the SPCE can be integrated with an electrochemical analytic system for label-free chemical and biological detection.

Acknowledgements

This study was supported by Ministry of Science and Technology under contracts (MOST 103-2113-M-018-001-MY2). We thank Wallace Academic Editing for the English language editing.

Notes and references

Department of Chemistry, National Changhua University of Education,1, Jin-De Road, Changhua City, Taiwan; Tel: 011-886-4-7232105-3522

E-mail: linywjerry@cc.ncue.edu.tw

Electronic Supplementary Information (ESI) available: [Figure S1. EDS spectra-, Figure S2. HRXRD spectra-, Figure S3. SALDI-MS spectra-, Figure S4. XPS spectra of the irregularly shaped Ag particles and desert-rose-like Ag mesoparticles. Figure S5. The desert-rose-like Ag mesoparticles at various electrodeposition times. Figure S6. Electrodeposition time, roughness factor, and Raman intensity of the desert-rose-like Ag mesoparticles. Figure S7. Ag structures prepared in different electrolytes. Figure S8. SEM images and SERS spectra of 4-MBA molecules adsorbed onto Ag substrates prepared in different electrolytes. Figure S9. TEM images of depsotion solutions containg Au NP suspensions. Figure S10. SEM images and SERS spectra of 4-MBA molecules adsorbed onto different Ag substrates. Figure S11. Optimal condition for Raman intensity of 4-MBA. Figure S12. Raman mapping of 4-MBA on Ag substrates. Figure S13. Raman spectra of 4-MBA on irregularly shaped Ag particles at 80 °C. Figure S14. SEM images and Raman spectra of 4-MBA on Ag structures at various temperatures. Figure S15. The aging behaviors of the SERS active substrate. Figure S16. Raman spectra of DMAB and DTNB molecules.]. See DOI: 10.1039/b000000x/

1. P. P. Fang, X. H. Lu, H. Liu and Y. X. Tong, *Trend. Anal. Chem.*, 2015, **66**, 103-117.
2. L. B. Yang, P. Li, H. L. Liu, X. H. Tang and J. H. Liu, *Chem. Soc. Rev.*, 2015, **44**, 2837-2848.
3. Q. Liu, Q. F. Zhou and G. B. Jiang, *Trend. Anal. Chem.*, 2014, **58**, 10-22.
4. M. Sezer, J. J. Feng, H. K. Ly, Y. F. Shen, T. Nakanishi, U. Kuhlmann, P. Hildebrandt, H. Mohwald and I. M. Weidinger, *Phys. Chem. Chem. Phys.*, 2010, **12**, 9822-9829.
5. J. A. Dougan and K. Faulds, *Analyst*, 2012, **137**, 545-554.
6. V. Turzhitsky, L. Qiu, I. Itzkan, A. A. Novikov, M. S. Kotelev, M. Getmanskiy, V. A. Vinokurov, A. V. Muradov and L. T. Perelman, *Appl. Spectrosc.*, 2014, **68**, 133-154.
7. C. J. Orendorff, A. Gole, T. K. Sau and C. J. Murphy, *Anal. Chem.*, 2005, **77**, 3261-3266.
8. Y. F. Shen, J. B. Wang, U. Kuhlmann, P. Hildebrandt, K. Ariga, H. Mohwald, D. G. Kurth and T. Nakanishi, *Chem-Eur. J.*, 2009, **15**, 2763-2767.
9. J. H. Kim, T. Kang, S. M. Yoo, S. Y. Lee, B. Kim and Y. K. Choi, *Nanotechnology*, 2009, **20**.
10. A. Gutes, C. Carraro and R. Maboudian, *ACS App. Mater. Inter.*, 2009, **1**, 2551-2555.
11. Y. Su, Q. He, X. H. Yan, J. B. Fei, Y. E. Cui and J. B. Li, *Chem-Eur. J.*, 2011, **17**, 3370-3375.
12. Y. Y. Xia, T. J. Li, C. Gao, C. Ma and J. Chen, *J. Mater. Sci.*, 2014, **49**, 2781-2786.
13. M. Murphy, K. Ting, X. L. Zhang, C. Soo and Z. Zheng, *J. Nanomater.*, 2015.
14. M. Shah, V. Badwaik, Y. Kherde, H. K. Waghwani, T. Modi, Z. P. Aguilar, H. Rodgers, W. Hamilton, T. Marutharaj, C. Webb, M. B. Lawrenz and R. Dakshinamurthy, *Front. Biosci.-Landmrk.*, 2014, **19**, 1320-U1274.
15. J. Lee, E. Y. Park and J. Lee, *Bioproc. Biosyst. Eng.*, 2014, **37**, 983-989.
16. C. D. Gu, X. J. Xu and J. P. Tu, *J. Phys. Chem. C*, 2010, **114**, 13614-13619.
17. C. Gu and T. Y. Zhang, *Langmuir*, 2008, **24**, 12010-12016.
18. C. Gu, H. Ren, J. Tu and T. Y. Zhang, *Langmuir*, 2009, **25**, 12299-12307.
19. Y. W. Lin, W. T. Chen and H. T. Chang, *Rapid Commun Mass Sp*, 2010, **24**, 933-938.
20. Y. F. Huang, Y. W. Lin, Z. H. Lin and H. T. Chang, *J. Nanopart. Res.*, 2009, **11**, 775-783.
21. A. Michota and J. Bukowska, *J. Raman Spectrosc.*, 2003, **34**, 21-25.
22. C. E. Taylor, J. E. Pemberton, G. G. Goodman and M. H. Schoenfisch, *Appl. Spectrosc.*, 1999, **53**, 1212-1221.
23. M. Yang, R. Alvarez-Puebla, H. S. Kim, P. Aldeanueva-Potel, L. M. Liz-Marzan and N. A. Kotov, *Nano Lett.*, 2010, **10**, 4013-4019.
24. L. Rodriguez-Lorenzo, R. A. Alvarez-Puebla, I. Pastoriza-Santos, S. Mazzucco, O. Stephan, M. Kociak, L. M. Liz-Marzan and F. J. G. de Abajo, *J. Am. Chem. Soc.*, 2009, **131**, 4616-4618.
25. X. S. Shen, G. Z. Wang, X. Hong and W. Zhu, *Phys. Chem. Chem. Phys.*, 2009, **11**, 7450-7454.
26. L. Cheng, C. S. Ma, G. Yang, H. J. You and J. X. Fang, *J. Mater. Chem. A*, 2014, **2**, 4534-4542.
27. H. You, S. Yang, B. Ding and H. Yang, *Chem Soc Rev*, 2013, **42**, 2880-2904.
28. J. X. Fang, S. Y. Du, S. Lebedkin, Z. Y. Li, R. Kruk, M. Kappes and H. Hahn, *Nano Lett.*, 2010, **10**, 5006-5013.
29. C. C. Chang, K. H. Yang, Y. C. Liu, T. C. Hsu and F. D. Mai, *ACS App. Mater. Inter.*, 2012, **4**, 4700-4707.
30. N. Crivillers, M. Mas-Torrent, J. Vidal-Gancedo, J. Veciana and C. Rovira, *J. Am. Chem. Soc.*, 2008, **130**, 5499-5506.
31. S. Bollo, C. Yánez, J. Sturm, L. Nunez-Vergara and J. A. Squella, *Langmuir*, 2003, **19**, 3365-3370.
32. M. Weisser, G. Nelles, P. Wohlfart, G. Wenz and S. Mittler-Neher, *J. Phy. Chem.*, 1996, **100**, 17893-17900.
33. K. W. Kho, Z. X. Shen, Z. Lei, F. Watt, K. C. Soo and M. Olivo, *Anal. Chem.*, 2007, **79**, 8870-8882.
34. H.-P. Chiang, P. Leung and W. Tse, *J. Phys. Chem. B*, 2000, **104**, 2348-2350.
35. Y. S. Pang, H. J. Hwang and M. S. Kim, *J. Phys. Chem. B*, 1998, **102**, 7203-7209.
36. L. B. Zhao, Y. F. Huang, D. Y. Wu and B. Ren, *Acta Chim. Sinica*, 2014, **72**, 1125-1138.
37. C. W. Liu, Y. W. Lin, C. C. Huang and H. T. Chang, *Biosens. Bioelectron.*, 2009, **24**, 2541-2546.

